Layer-Dependent Giant Magnetoresistance in Two-Dimensional $CrPS_4$ Magnetic Tunnel Junctions

Jie Yang,[1] Shibo Fang,[1] Yuxuan Peng,[1] Shiqi Liu,[1] Baochun Wu,[1] Ruge Quhe,[2] Shilei Ding,[1] Chen Yang,[1] Jiachen Ma,[1] Bowen Shi,[1] Linqiang Xu,[1] Xiaotian Sun,[3] Guang Tian,[1] Changsheng Wang,[1,4] Junjie Shi,[1,4,5] Jing Lu,[1,4,5,6,*] and Jinbo Yang[1,4,5,6,†]

[1] *State Key Laboratory for Mesoscopic Physics and School of Physics, Peking University, Beijing 100871, People's Republic of China*

[2] *State Key Laboratory of Information Photonics and Optical Communications and School of Science, Beijing University of Posts and Telecommunications, Beijing 100876, People's Republic of China*

[3] *College of Chemistry and Chemical Engineering, and Henan Key Laboratory of Function-Oriented Porous Materials, Luoyang Normal University, Luoyang 471934, People's Republic of China*

[4] *Collaborative Innovation Center of Quantum Matter, Beijing 100871, People's Republic of China*

[5] *Peking University Yangtze Delta Institute of Optoelectronics, Nantong 226010, People's Republic of China*

[6] *Beijing Key Laboratory for Magnetoelectric Materials and Devices (BKL-MEMD), Peking University, Beijing 100871, People's Republic of China*

(Received 1 April 2021; revised 27 June 2021; accepted 19 July 2021; published 6 August 2021)

Antiferromagnetism within the two-dimensional (2D) family offers a platform for spintronics. The emergent 2D semiconductor $CrPS_4$ is proved to be composed of ferromagnetic layers with antiferromagnetic coupling along the stacking direction in the experiment. By using the first-principles quantum-transport simulation, we evaluate the spin-resolved transport in the magnetic tunnel junction built by the 2D $CrPS_4$ tunnel barrier with large thickness ranges. We find the magnetoresistance generally increases with the number of tunnel layers from 140% (three layers) to a surprising 370 000% (10 layers). An odd-even oscillation magnetoresistance behavior exists in few layers due to the electrode option. Our results will inspire further experimental verification and provide vital insights for 2D spintronics design.

DOI: 10.1103/PhysRevApplied.16.024011

I. INTRODUCTION

Current magnetic memory and processing mainly built by magnetic tunneling junctions (MTJs) are out of reaching the two-dimensional (2D) van der Waals (vdW) materials' family due to the absence of a magnetic target [1]. However, the discovery of long-range magnetic order in atomic layers, such as $Cr_2Ge_2Te_6$ [2], CrX_3 (X = Cl, I, Br) [3–7], Fe_3GeTe_2 [8,9], and CrSBr [10], is regarded as a milestone in establishing the 2D memory revolution [6]. Compared with the traditional deposited thin-film insulator represented by MgO, the competitiveness of the 2D magnetic materials lies in the following aspects. First, the surface of the 2D materials is uniform and free of dangling bonds [4]. Such a surface gives rise to sharp spin-resolved states' distribution at the interface between the electrode and tunnel region, diminishes the band broadening, and keeps the magnetism as intrinsic as possible [11]. Besides, a uniform surface results in a uniform barrier thickness, which facilitates all-area tunneling. By contrast, tunneling in nonuniform MTJs preferentially passes through the thinner barrier regions in terms of the exponential decay of the tunneling current with the barrier thickness [1]. Second, the weak interlayer magnetic coupling in the 2D materials allows a continuous MTJ unit array featured by a low critical magnetic field for a transition from the antiferromagnetic coupling to ferromagnetic coupling, and the MTJ array can dramatically amplify the magnetoresistance [11,12]. For example, the experimentally observed magnetoresistance in the bilayer, trilayer, 4-layer, and 10-layer CrI_3 MTJ reaches approximately 95%, 300%, 550%, and over 1 000 000%, respectively [4,13]. The last one far exceeds the record of the traditional MgO-based MTJs (at most approximately 1000% at low temperature) [4,12–15]. Third, the extremely small thickness of the 2D materials benefits by minimizing the size of the unit memory cell and deeply improves the memory device integration [16,17]. All of the development pushes the class of 2D magnetic materials to play promising roles in the stage of next-generation spintronics [16,18].

*jinglu@pku.edu.cn
†jbyang@pku.edu.cn

As ternary transition metal chalcogenides, $CrPS_4$ crystal was synthesized in the 1970s, but its magnetic order is just clarified [18–23]. It is confirmed as an A-type antiferromagnet with the intralayer ferromagnetic interaction and interlayer antiferromagnetic coupling along the stacking direction below 38 K by the method of neutron diffraction, in agreement with the theoretical proposed magnetic structures [24–26]. Bulk $CrPS_4$ is a semiconductor with a band gap of approximately 1.3 eV through optical measurement and approximately 0.8 eV through first-principles calculation [20,25]. The semiconducting behavior maintains until the thickness scales down to the monolayer [20]. The interlayer antiferromagnetic order and semiconducting property make 2D $CrPS_4$ desirable for atomically spintronic devices just like 2D CrI_3 does. Recently, 2D $CrPS_4$ with thickness ranging from monolayer to several layers are successfully exfoliated in the experiment [20,27]. However, studies on transport and device building based on 2D $CrPS_4$ are still blank at present.

In this work, we investigate the tunneling magnetoresistance (TMR) as a function of the $CrPS_4$ layer thickness from bilayer to ten layers in the $CrPS_4$-based MTJs via *ab initio* quantum-transport calculation. Giant TMR is revealed and has an increasing tendency with the thickness of $CrPS_4$. To be specific, the TMR first experiences a prominent odd-even effect ranging from 140% to a giant approximate 13 000% within the 7-layer $CrPS_4$ and then monotonically rises up to a surprising value of 370 000% when the tunnel thickness accumulates to 10 layers. The TMR level is much higher than other theoretical reports based on the 2D MTJ configuration with several tunnel layers [5,28–32].

II. METHODOLOGY

The spin-dependent transport properties are calculated by using the density functional theory (DFT) coupled with the nonequilibrium Green's function (NEGF) formalism, as implemented in the Atomistix ToolKit 2018 software package [33,34]. The exchange-correlation interaction is described by spin-polarized generalized gradient approximation with the Hubbard U (SGGA + U) in the form of the Perdew-Burke-Ernzerhof (PBE) potential [35,36]. The effective Hubbard U parameter ($U = 3$ eV) is applied for Cr d states in our quantum-transport calculations [25]. The double zeta polarized (DZP) set is used. The real-space mesh cutoff is taken as 155 Hartree. The k-point meshes for the electrode region and the central region are $35 \times 35 \times 15$ and $35 \times 35 \times 1$, respectively. The boundary conditions in the electrode region (central region) are period-, period-, and period-type (Dirichlet-type) conditions along x, y, and z directions (z is the transport direction). The temperature is at 0 K. The electronic structures calculations are carried out in the Vienna *ab initio* simulation package [35]. The energy cutoff for the plane-wave expansion is 500 eV. The vacuum space is larger than 20 Å. The Monkhorst-Pack k-point mesh is sampled with a separation of about 0.02 $Å^{-1}$ in the Brillouin zone [37]. The DFT-D2 correction is chosen to consider the vdW interaction.

The transmission coefficient $T_\sigma^{k_\parallel}(E)$ ($k_\parallel$ stands for the reciprocal lattice vector along the surface-parallel direction in the irreducible Brillouin zone, σ is the spin index) is represented by [38,39]

$$T_\sigma^{k_\parallel}(E) = Tr[\Gamma_{l,\sigma}^{k_\parallel}(E)\, G_\sigma^{k_\parallel}(E)\, \Gamma_{r,\sigma}^{k_\parallel}(E)\, G_\sigma^{k_\parallel\dagger}(E)], \quad (1)$$

where $G_\sigma^{k_\parallel}(E)$ and $G_\sigma^{k_\parallel\dagger}(E)$ stand for the retard and advanced Green's function, respectively.

$$G_\sigma^{k_\parallel}(E) = \frac{1}{(E + i\delta_+)I - H^{k_\parallel} - \sum_{l,\sigma}^{k//}(E) - \sum_{r,\sigma}^{k//}(E)}, \quad (2)$$

where δ_+ is an infinitesimal positive number, I the identity matrix, $H^{k_\parallel}$ the Hamiltonian matrix, and $\sum_{l/r,\sigma}^{k_\parallel}(E)$ the self-energy matrix [40]. $\Gamma_{l/r,\sigma}^{k_\parallel}(E) = i(\sum_{l/r,\sigma}^{k_\parallel} - \sum_{l/r,\sigma}^{k_\parallel\dagger})$ is the broadening width stemming from left and right electrodes in the form of self energy. Given certain energy, $T_\sigma^{k_\parallel}(E)$ is averaged over all different $k_\parallel$.

III. RESULTS AND DISCUSSION

Bulk $CrPS_4$ possesses monoclinic symmetry (space group $C2$). The primitive lattice constants are $a = b = 6.526$ Å, $c = 6.135$ Å, $\alpha = \beta = 91.567°$, $\gamma = 67.450°$. Each Cr atom is surrounded by six S atoms and located at the center of this distorted octahedron. The P atom is coordinated in the center of three CrS_6 octahedra [Figs. 1(a) and 1(b)] [18]. The calculated magnetic moments of each Cr atom are approximately $3.14\mu_B$, independent of the magnetic orders and layer number. The spin-resolved band structures of 2D $CrPS_4$ from bilayer to ten layers are shown in Fig. 1 (2–3 layer) and Fig. 9 (4–10 layer). The band dispersions in the FM state are similar for different layer $CrPS_4$. The AFM state band structures are degenerate for even layer $CrPS_4$. The AFM band dispersions for odd layer $CrPS_4$ are almost degenerate around the Fermi level but become spin recognizable in the deep energy zone. The spin- and layer-dependent band gaps of 2D $CrPS_4$ are summarized in Table I.

The calculated antiferromagnetic (AFM) and ferromagnetic (FM) band structures of the magnetic primitive cell of bulk $CrPS_4$ are shown in Figs. 1(c) and 1(d). Their corresponding band gaps are 0.83 eV (antiferromagnetic state), 0.72 eV (spin up in the FM state), and 1.43 eV (spin down in the FM state), respectively. The cohesive energy in the FM state is 2.25 meV per Cr atom higher than the AFM state, implying the critical magnetic field of

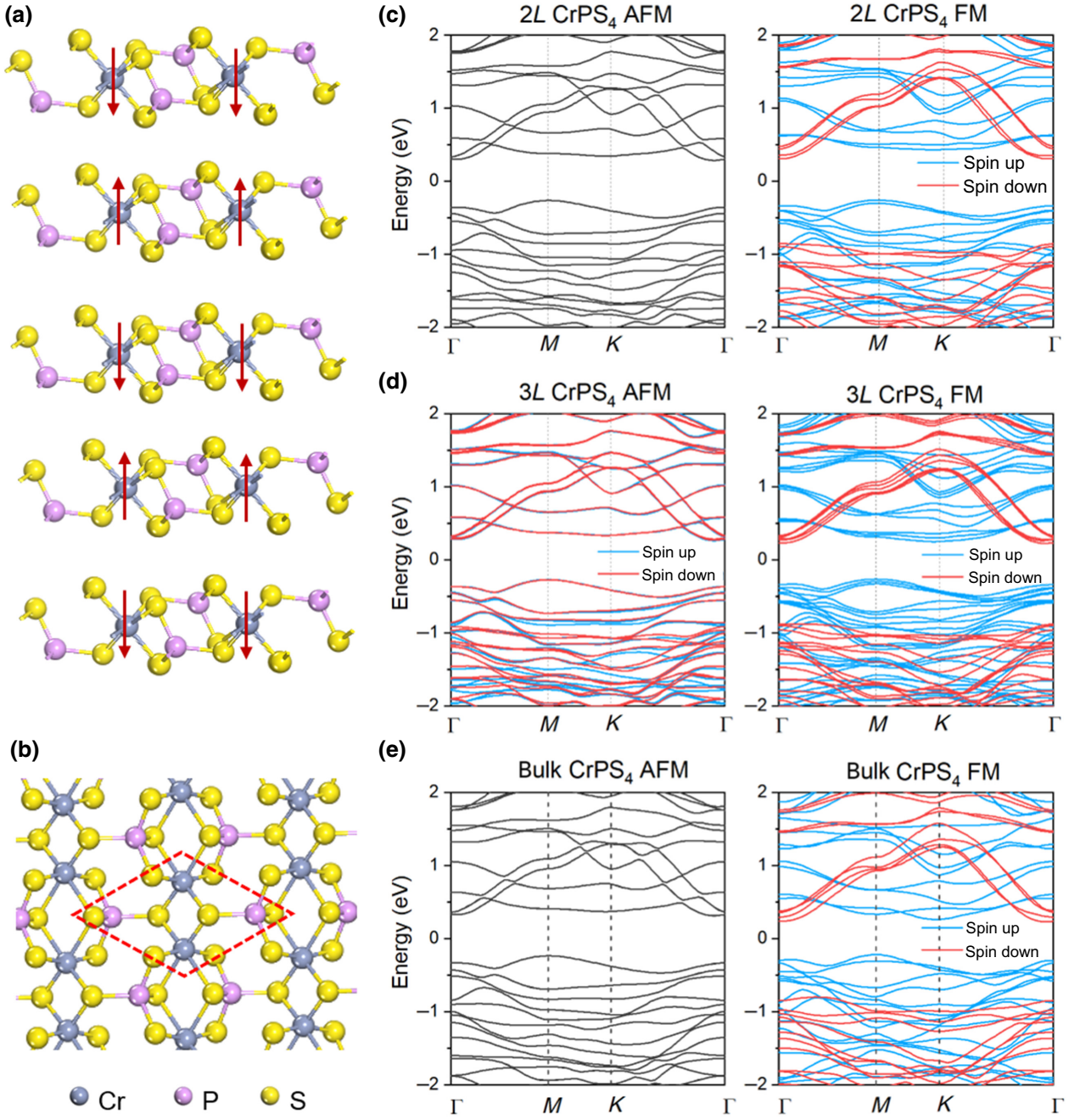

FIG. 1. Lattice and electronic structures of $CrPS_4$. The top (a) and side (b) view of bulk $CrPS_4$. The arrows represent the magnetic moments in each layer. The red dash parallelogram is the primitive lattice. (c)–(e) Spin-dependent band structures for bilayer, 3-layer, and bulk $CrPS_4$ in the AFM and FM states. A $1 \times 1 \times 2$ supercell is applied to calculate the bulk band structures.

approximately 12 T ($m \cdot H_c = \Delta E$, $m = 3\mu_B$) to completely switch antiferromagnetism to ferromagnetism. The experimental spin-flip transition of the $CrPS_4$ single crystal from the AFM to FM order starts from approximately 0.8 T and completes at 8 T [24].

We use five-layer Au (111) to substitute semi-infinite Au metal contacting with 2D $CrPS_4$ to make geometry optimization (Fig. 10). After completing optimization, Au in two ends of the heterostructure is extended to the semi-infinite electrode of the MTJ device. The distortion of Au atoms in the device model is caused by the full relaxation of all Au atoms. Since Au is used for providing electrons, we speculate that the deformation would not change the order of magnitude of our results. Further confirmation details and a comparison of different relaxation ways are included in the Appendix. The effect of different relaxation ways (partial relaxation and complete relaxation) of the Au electrode on the TMR

is negligible compared with the layer-dependent scaling behavior.

The conductance of the configuration is different when the interlayer magnetic coupling in $CrPS_4$ is AFM or FM [14]. Gold is chosen because it is one of the most commonly used electrodes in the experiment. G_{FM} and G_{AFM} are the conductance of the junction when $CrPS_4$ is in the FM and the AFM order, respectively, and are calculated as

$$G_{FM} = \frac{e^2}{h}(T_{FM,\uparrow}(E) + T_{FM,\downarrow}(E)),$$
$$G_{AFM} = \frac{e^2}{h}(T_{AFM,\uparrow}(E) + T_{AFM,\downarrow}(E)) \quad (3)$$

at $E = E_f$. T_{FM} and T_{AFM} are the transmission coefficient in the FM and AFM states, respectively. At a low bias and zero bias, the conductance is proportional to the transmission coefficient $T(E_f)$. P_{FM} and P_{AFM} are the spin polarization (P) of the junction in the FM and AFM states [Fig. 2(c)]. At zero bias, P is calculated as

$$P_{FM} = (T_{FM,\uparrow}(E) - T_{FM,\downarrow}(E))/(T_{FM,\uparrow}(E) + T_{FM,\downarrow}(E)),$$
$$P_{AFM} = (T_{AFM,\uparrow}(E) - T_{AFM,\downarrow}(E))/(T_{AFM,\uparrow}(E) + T_{AFM,\downarrow}(E)) \quad (4)$$

at $E = E_f$. Since the spin-resolved band edges of the $CrPS_4$ in the FM and AFM states are different, electrons with different spins will experience different barrier heights when tunneling. As the band structures in Figs. 1(c) and 1(d) shows, in the FM state, since the spin-down electrons (the minority) see a high barrier, and the spin-up (the majority) electrons see a low barrier, the majority electrons would

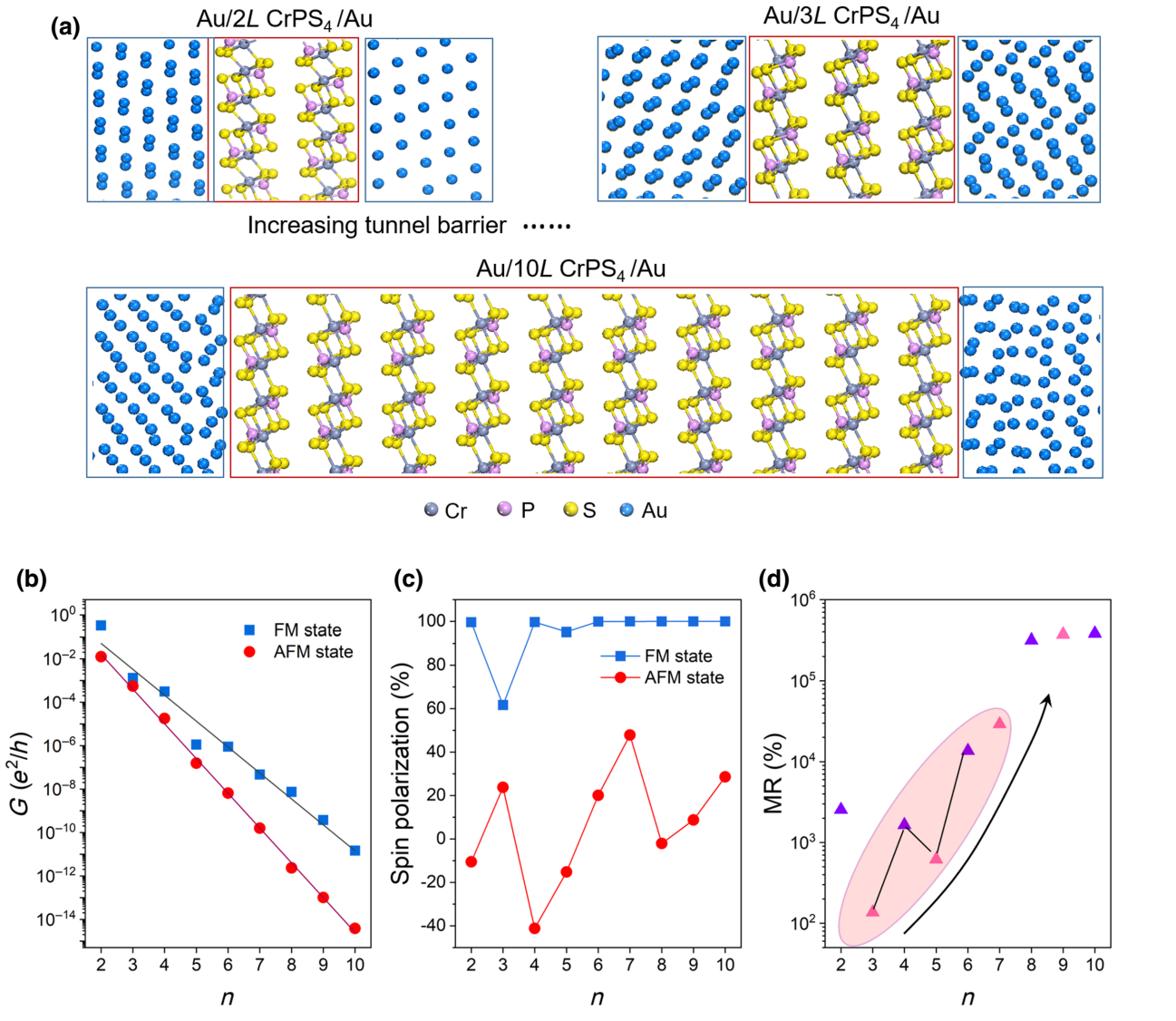

FIG. 2. (a) Device model of the Au/n-layer $CrPS_4$/Au magnetic tunnel junction. The conductance (b) and spin polarization (c) in the FM and AFM states, and TMR in a log scale (d) as a function of the $CrPS_4$ layer number n.

pass the barrier but the minority electrons would not, leading to a high G and a high P. By contrast, in the AFM state, since both the spin-up and -down electrons see the same high barrier, they hardly pass the barrier, leading to a low G and a low P [41]. Namely, G_{FM} is higher than G_{AFM}, and P_{FM} is larger than P_{AFM}, the same as our calculated results in Figs. 2(b) and 2(c). As the tunnel barrier becomes thick, G of this junction in the FM and AFM states linearly decreases. The relation between G_{FM} (G_{AFM}) and thickness l is well fitted with $\log G_{\mathrm{FM}} = 1.09d - 1.19(e^2/h)$ and $\log G_{\mathrm{AFM}} = 1.40d - 1.60(e^2/h)$, respectively. The decreasing G also positively relates to the corresponding $k_{\parallel}$-resolved transmission coefficients of the $CrPS_4$-based MTJs with different tunnel barrier thicknesses in Fig. 4. We discuss it later. The P_{FM} shows odd-even oscillation ranging from 60% to 100% (tunnel layer number < 7) and then maintains 100% (tunnel layer number ≥ 7). The P_{AFM} fluctuates in the range of −40%–40% when the tunnel layer number increases from 2 to 10.

The TMR is defined as $\mathrm{TMR} = (G_{\mathrm{FM}} - G_{\mathrm{AFM}})/G_{\mathrm{AFM}} \times 100\%$. The calculated TMR is summarized in Fig. 2(d). We find that the TMR tends to increase with the tunnel layer number. To be specific, the TMR displays different layer dependence when the tunnel layer number is less or larger than 6. When the tunnel layer number is less than 6, the TMR (137%–13 657%) increases when the tunnel layer number increases in the odd or even sequence (except the bilayer case), but the TMR oscillates with the adjacent odd-even tunnel layer number. We find that the Au/2–6-layer $CrPS_4$/Au MTJs with the $2n$-layer tunnel barrier (assuming n is an integer and $2n < 7$) have higher TMR than that one with the $2n+1$-layer tunnel barrier ($2n+1$ is odd). For example, the TMR in the Au/4-layer $CrPS_4$/Au MTJ is 1649%, larger than 619% of the Au/5-layer $CrPS_4$/Au MTJ.

As the tunnel barrier thickness increases to more than 6 layers, the TMR's odd-even oscillation in our $CrPS_4$-based MTJs disappears. We do not pursue the TMR beyond the 10 tunneling layers. First, the tunnel film thickness in the traditional MTJs has to be controlled within a certain scope to guarantee an effective tunnel. For example, the thickness of the MgO tunnel barrier film used in the Co-Fe-B/MgO MTJs is less than 3 nm in the experiment [15]. The thickness of the tunnel region in our Au/6-layer $CrPS_4$/Au MTJs exceeds 3 nm, the experimental film scale, and in the Au/10-layer $CrPS_4$/Au MTJ approaches approximately 5.6 nm. Second, as the tunnel barrier gets thick, the transport probabilities would exponentially decrease even beyond the simulated accuracy, which makes the results no sense. The transmission coefficient of the graphite/8-layer/graphite MTJ at the AFM state vanishes at the Fermi level at the Γ point. Third, the calculation burden becomes heavy and exceeds the computational capability. Finally, as the function of the TMR versus n in Fig. 2(d) shows, the TMR tends to be saturated at approximately 10^5% when $n = 8$–10. The TMR's increase rate in $n = 9$ and 10 are 18% and 2%, respectively, far less than the order of magnitude increase from $n = 3$ to 8. Therefore, we can estimate the large n limit from the TMR value at $n = 10$. Namely, the TMR at the large n limit is estimated to be 10^5%.

A further relationship between the TMR and the tunnel thickness needs to be discussed. Using Wentzel-Kramers-Brillouin (WKB) approximation, the tunneling transport possibility (T) is [42]

$$T = \exp\left(-2\int \frac{dx\sqrt{2\mu[U - E_f + B(x)\cdot\sigma]}}{\hbar}\right). \quad (5)$$

Here $B(x)$ is the x-dependent magnetic field, σ the spin index, μ the effective mass of a free electron, $(U - E_f)$ the tunnel barrier height in the nonmagnetic system, and $\hbar$ Plank's constant. The conductance is given by

$$G = A\sum |T|^2, \quad (6)$$

where A is a constant. We can get G_{FM} and G_{AFM},

$$G_{\mathrm{FM}} = A\left[\exp\left(-4\int_0^l \frac{dx\sqrt{2\mu[U - E_f + B_{\mathrm{FM}}(x)\cdot\sigma]}}{\hbar}\right) + exp\left(-4\int_0^l \frac{dx\sqrt{2\mu[U - E_f - B_{\mathrm{FM}}(x)\cdot\sigma]}}{\hbar}\right)\right], \quad (7)$$

$$G_{\mathrm{AFM}} = A\left[\exp\left(-4\int_0^l \frac{dx\sqrt{2\mu[U - E_f + B_{\mathrm{AFM}}(x)\cdot\sigma]}}{\hbar}\right) + exp\left(-4\int_0^l \frac{dx\sqrt{2\mu[(U - E_f - B_{\mathrm{AFM}}(x)\cdot\sigma)]}}{\hbar}\right)\right], \quad (8)$$

where l is the tunnel thickness. After using Taylor expansion,

$$\int_0^l dx\sqrt{[U - E_f + B(x)\cdot\sigma]} = \int_0^l dx\sqrt{(U - E_f)} + \int_0^l dx\frac{B(x)\cdot\sigma}{\sqrt{(U - E_f)}}. \quad (9)$$

The TMR becomes

$$\begin{aligned}\mathrm{TMR} &= \frac{G_{\mathrm{FM}} - G_{\mathrm{AFM}}}{G_{\mathrm{AFM}}} \\ &= \frac{\exp\left(-\frac{2}{\hbar}\int dx\frac{\sqrt{B_{\mathrm{FM}}(x)\cdot\sigma}}{\sqrt{(U-E_f)}}\right) + \exp\left(\frac{2}{\hbar}\int dx\frac{\sqrt{B_{\mathrm{FM}}(x)\cdot\sigma}}{\sqrt{(U-E_f)}}\right) - \exp\left(-\frac{2}{\hbar}\int dx\frac{\sqrt{B_{\mathrm{AFM}}(x)\cdot\sigma}}{\sqrt{(U-E_f)}}\right) - \exp\left(\frac{2}{\hbar}\int dx\frac{\sqrt{B_{\mathrm{AFM}}(x)\cdot\sigma}}{\sqrt{(U-E_f)}}\right)}{\exp\left(\frac{2}{\hbar}\int dx\frac{\sqrt{B_{\mathrm{AFM}}(x)\cdot\sigma}}{\sqrt{(U-E_f)}}\right) + \exp\left(\frac{2}{\hbar}\int dx\frac{\sqrt{B_{\mathrm{AFM}}(x)\cdot\sigma}}{\sqrt{(U-E_f)}}\right)}.\end{aligned} \tag{10}$$

According to the Heisenberg model,

$$\int_0^l B(x)\cdot\sigma \;= \sum\nolimits_i J_i(x)\; S_i\cdot\sigma \;+ \sum\nolimits_j J_j(x)\; S_j\cdot\sigma. \tag{11}$$

Here i and j are the index of the current layer and the adjacent layers, respectively. S_i (S_j) and J_i (J_j) are the spin operator and the exchange coupling within one layer (between the adjacent layers), respectively.

When $l = 2na$ (even layer), n is an integer, and a the width of each layer,

$$\begin{aligned}\int_0^l dx\frac{B_{\mathrm{FM}}(x)\cdot\sigma}{\sqrt{(U-E_f)}} &= \frac{2a}{\sqrt{(U-E_f)}}\left(J_i\sum_i S_i + J_j\sum_j S_j\right)\cdot\sigma + \frac{(2n-2)a}{\sqrt{(U-E_f)}}\left(J_i\sum_i S_i + J_j\sum_j S_j\right)\cdot\sigma, \\ &= \frac{a}{\sqrt{(U-E_f)}}\left[2\sum_i J_iS_i + 2\sum_j J_jS_j + (2n-2)\sum_i J_iS_i + (4n-4)\sum_j J_jS_j\right]\cdot\sigma,\end{aligned} \tag{12}$$

$\int_0^l dx\frac{B_{\mathrm{AFM}}(x)\cdot\sigma}{\sqrt{(U-E_f)}} = 0$ (the details are located behind the main body)

$$\begin{aligned}\therefore \mathrm{TMR}^{\mathrm{even}} &= \frac{\exp\left(-\frac{2}{\hbar}\int dx\frac{B_{\mathrm{FM}}(x)\cdot\sigma}{\sqrt{(U-E_f)}}\right) + \exp\left(\frac{2}{\hbar}\int dx\frac{B_{\mathrm{FM}}(x)\cdot\sigma}{\sqrt{(U-E_f)}}\right) - 2}{2}, \\ &= \frac{cosh\left\{\frac{2a}{\hbar(U-E_f)}\left[2\sum_i J_iS_i + 2\sum_j J_jS_j + (2n-2)\sum_i J_iS_i + (4n-4)\sum_j J_jS_j\right]\right\} - 2}{2}.\end{aligned} \tag{13}$$

When $l = (2n-1)a$ (odd layer) and n is an integer, larger than 2,

$$\begin{aligned}\int_0^l dx\frac{B_{\mathrm{FM}}(x)\cdot\sigma}{\sqrt{(U-E_f)}} &= \frac{a}{\sqrt{(U-E_f)}}\left[2\sum_i J_iS_i + 2\sum_j J_jS_j + (2n-3)\sum_{iJ_i} S_i + (4n-6)\sum_j J_jS_j\right]\cdot\sigma, \\ \int_0^d dx\frac{B_{\mathrm{AFM}}(x)\cdot\sigma}{\sqrt{(U-E_f)}} &= \frac{a}{\sqrt{(U-E_f)}}\sum_i J_iS_i\cdot\sigma\end{aligned} \tag{14}$$

$$\therefore \mathrm{TMR}^{\mathrm{odd}} = \frac{cosh\left\{\frac{2a}{\hbar(U-E_f\ )}\left[2\sum_i J_iS_i + 2\sum_j J_jS_j + (2n-3)\sum_i J_iS_i + (4n-6)\sum_j J_jS_j\right]\right\} - G_{\mathrm{AFM}}}{G_{\mathrm{AFM}}}. \tag{15}$$

And $G_{\mathrm{AFM}} = cosh\left(\frac{a}{\sqrt{(U-E_f)}}\sum_i J_iS_i\cdot\sigma\right)$, which is irrelevant to n.

All unmarked range of integration is from 0 to the tunnel thickness l. The function of $\mathrm{TMR}^{\mathrm{even}}$ ($\mathrm{TMR}^{\mathrm{odd}}$) versus d has the same monotonicity as the *cosh* function, which is widely known as a monotonically increasing function. In conclusion, the TMR increases with the tunnel layer thickness, in agreement with our calculation in Fig. 2(d).

We take a 4-layer $CrPS_4$ tunnel barrier to explain the equation of $\int_0^l dx \frac{B_{AFM}(x)\cdot\sigma}{\sqrt{(U-E_f)}} = 0$.

$$\begin{aligned}\int_0^{4a} dx \frac{B_{AFM}(x)\cdot\sigma}{\sqrt{(U-E_f)}} &= \int_0^{a} dx \frac{B_{AFM}(x)\cdot\sigma}{\sqrt{(U-E_f)}} + \int_a^{2a} dx \frac{B_{AFM}(x)\cdot\sigma}{\sqrt{(U-E_f)}} + \int_{2a}^{3a} dx \frac{B_{AFM}(x)\cdot\sigma}{\sqrt{(U-E_f)}} + \int_{3a}^{4a} dx \frac{B_{AFM}(x)\cdot\sigma}{\sqrt{(U-E_f)}},\\ &= \int_0^{a}\left[\sum_i J_i S_i\cdot\sigma - \sum_j J_j S_j\cdot\sigma\right]dx + \int_0^{2a}\left[-\sum_i J_i S_i\cdot\sigma + 2\sum_j J_j S_j\cdot\sigma\right]dx\\ &\quad + \int_{2a}^{3a}\left[\sum_i J_i S_i\cdot\sigma - 2\sum_j J_j S_j\cdot\sigma\right]dx + \int_{3a}^{4a}\left[-\sum_i J_i S_i\cdot\sigma + \sum_j J_j S_j\cdot\sigma\right]dx,\\ &= \frac{a}{\sqrt{(U-E_f)}}\left[2\sum J_1S_1 - \sum J_2S_2 - \sum J_1S_1 + 2\sum J_2S_2 + \ldots - \sum J_1S_1 + \sum J_2S_2\right]\cdot\sigma = 0.\end{aligned} \tag{16}$$

We also use graphite as the electrodes to build the 2–7-layer $CrPS_4$-based MTJs and calculate the TMR (Fig. 3), which does not show the odd-even behavior but increases with tunnel layer number n. Previous theoretical reports about the TMR of the $CrTe_2$/1–7 layers B-doped graphene/$CrTe_2$ MTJs, the $MnSe_2$/1–2 layers h-BN/$MnSe_2$ MTJs, and the CoFe/3–11 MgO layers/CoFe MTJs also increases with their tunnel layer thickness [43–45].

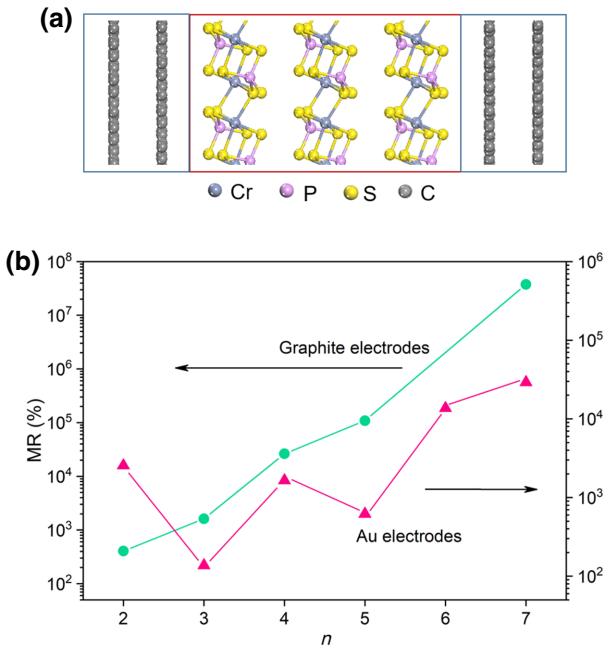

FIG. 3. (a) Device model of the graphite/2D $CrPS_4$/graphite MTJ. (b) Comparison of layer-dependent tunneling magnetoresistance of the graphite/n-layer $CrPS_4$/graphite and the Au/n-layer $CrPS_4$/Au (n is from 2 to 7) MTJs.

The odd-even TMR behavior blames the electrode option. To clearly reveal the deep reason, the spin-resolved LDOS (Figs. 4–6) in the FM and AFM states are plotted to make a comparison between the Au electrodes case and the graphite electrodes one. When $n = 2$ (Fig. 4), in the case of the Au electrode, due to the heavy interaction between Au and neighbor $CrPS_4$, there is complete metallization (spin-up channel) in the FM state and strong hybridization (two spin channels) in the AFM state. However, in the case of graphite electrodes, the mutual interaction between graphite and $CrPS_4$ is weak, and the band edges of 2L $CrPS_4$ and tunnel barriers are clear. When n increases to 3 (Fig. 5), in the case of Au electrodes, the G difference between the two states is small because their tunnel barriers (the FM spin-up channel and the AFM spin-down channel) are low and even the same, resulting in a degraded TMR. By contrast, in the case of graphite electrodes, the FM barrier height maintains while the AFM tunnel barrier number becomes more and would drastically reduce G_{AFM} and thus improve the TMR level. The barrier and the TMR with graphite electrodes also follow this rule when n increases to 4 (Fig. 6). As for the Au electrodes, the TMR is improved because the number of nonzero tunnel barriers in the AFM states is more. Considering the heavy interaction between Au and the adjacent $CrPS_4$, when the tunnel layer is not thick, it is hard to ignore the mutual $CrPS_4$ layers' hybridization, which obscures the barrier profile, reduces the difference between G_{FM} and G_{AFM}, and leads to a fluctuate TMR. When the tunnel barrier gets thick, the interlayer interaction gets weak, the barrier profile tends to become as uniform as that with graphite electrodes, and the TMR increases with n.

The Au/7-layer $CrPS_4$/Au MTJ is taken as an example to elucidate the tunneling pathways in thick tunnel layer. As the LDOS in Fig. 7 shows, the first and seventh $CrPS_4$ layers are highly metalized by Au electrodes in both the

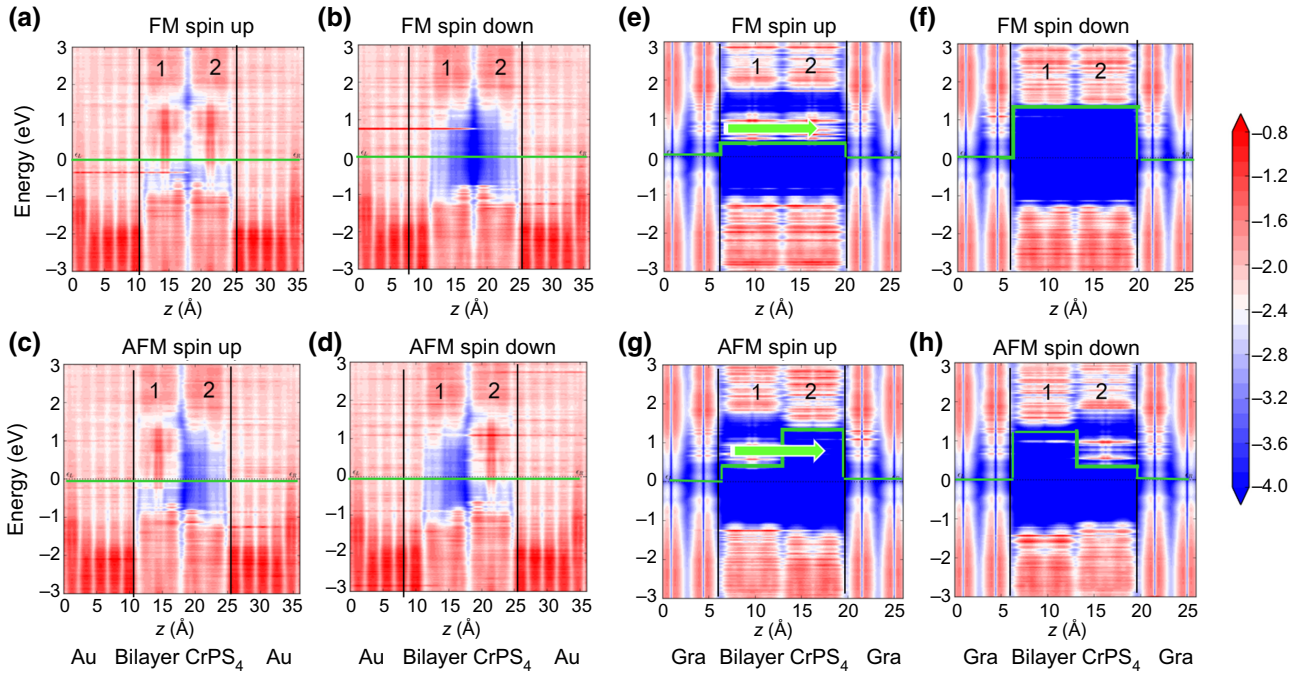

FIG. 4. Spin-resolved projected LDOS of the Au/bilayer $CrPS_4$/Au magnetic tunnel junction (a)–(d) and the graphite//bilayer $CrPS_4$/graphite magnetic tunnel junction (e)–(h).

FM or the AFM states [dashed circles in Fig. 7(a)], while other $CrPS_4$ layers have the obvious band gaps for two spins. Electrons with different spins suffer from different barriers after they pass the heavily hybridized states of the first $CrPS_4$ layer. In the FM state, the spin-dependent barrier is uniform. The barrier height is about 0.15 eV for the spin-up channel and about 1.13 eV for the spin-down channel. The total transmission probability is expected to

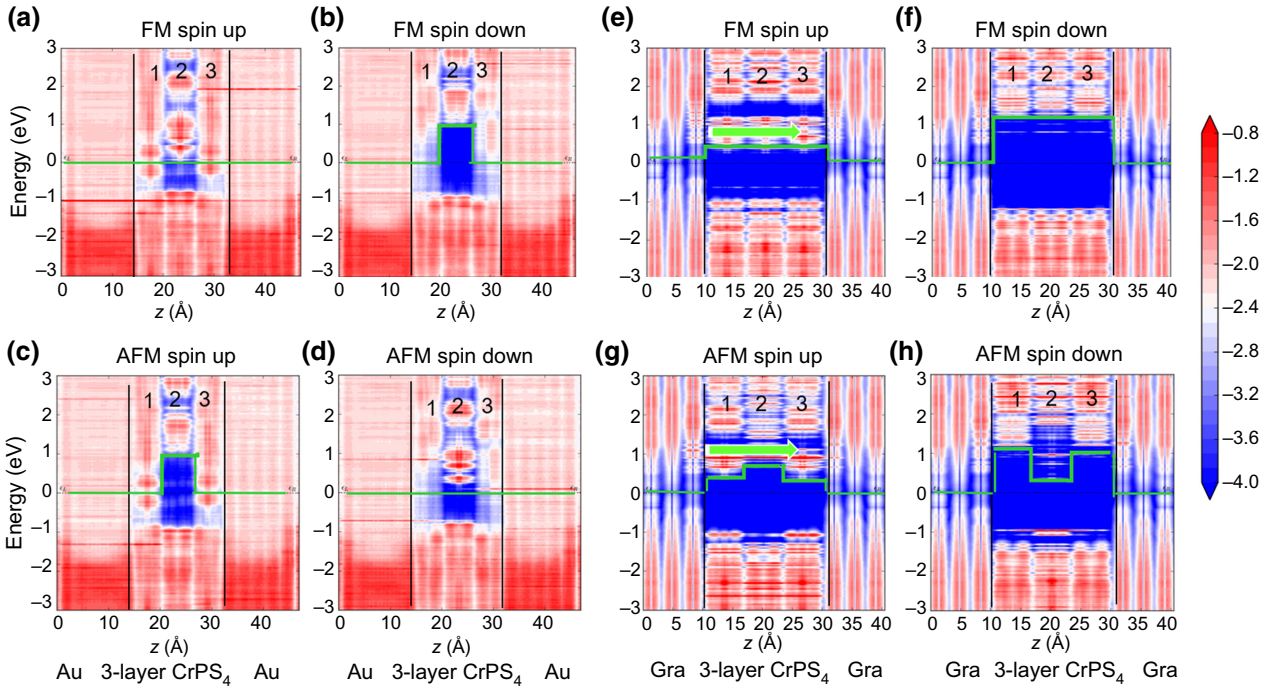

FIG. 5. Spin-resolved projected LDOS of the Au/3-layer $CrPS_4$/Au magnetic tunnel junction (a)–(d) and the graphite//3-layer $CrPS_4$/graphite magnetic tunnel junction (e)–(h).

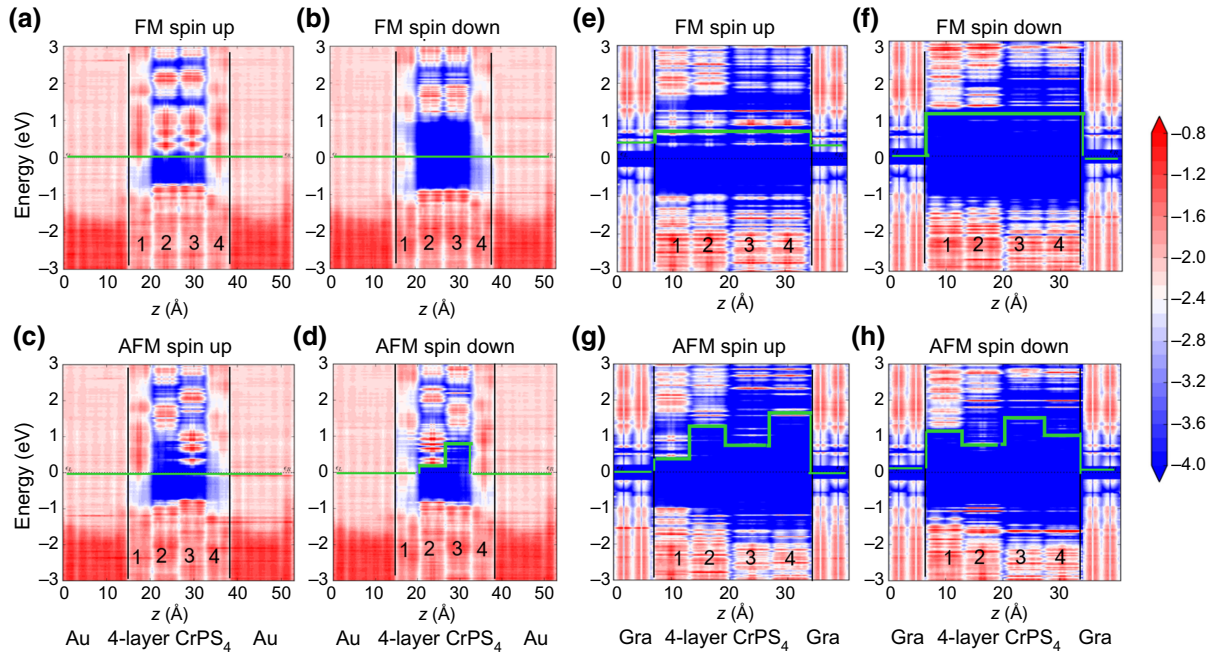

FIG. 6. Spin-resolved projected LDOS of the Au/4-layer $CrPS_4$/Au magnetic tunnel junction (a)–(d) and the graphite//4-layer $CrPS_4$/graphite magnetic tunnel junction (e)–(h).

be large as well as the conductance because the majority (spin-up) electrons face a small barrier. In the AFM state, the barrier height oscillates for two spin channels. Two spin electrons have to cross the barrier one by one: the barrier heights for the spin-up electrons are 1.14, 0.43, 1.14, 0.43, and 1.14 eV, respectively, and the barrier heights for the spin-down electrons are 0.22, 1.12, 0.22, 1.12, and 0.22 eV, respectively, when electrons depart from the left electrode. These barriers lead to a smaller total transmission probability in the AFM state than that of the FM state. As the thickness of the tunnel region increases, the transmission probability in the two states decreases because of the increasing width of the tunnel barrier. The transmission probability in the AFM state is much smaller because the number of the barriers is more. The transmission probability difference between two states becomes larger, and the TMR increases.

We also plot $k_{\parallel}$-resolved transmission across the Au/2D $CrPS_4$/Au MTJs with different tunnel layers for the FM and AFM states in the Brillouin zone (BZ) (Fig. 8). Γ is in the center of the BZ. The transmission distribution for the odd or even tunnel layer MTJs in the FM state is quite different, especially for the 3–6-layer cases: The highest transmission coefficient is located around the Γ point when the MTJ has odd tunnel layers. In contrast, the highest transmission coefficient in the BZ becomes marginalized when the MTJ has even tunnel layers. Besides, the area with high transmission coefficients in the case of the odd layer is larger than that of the even layer. As the tunnel region gets thicker (>7 layers), there is no apparent odd-even transmission difference. The transmission is reduced around the Γ point and maximizes in a certain peripheral region. The transmission in the AFM state has the same distribution as the corresponding FM counterpart but possesses a much smaller possibility. As the color bar in Fig. 8 shows, the transmission possibility reduces exponentially along with the increasing tunnel layers, in agreement with Eqs. (6) and (7) we declare and the lower G of the whole system in Fig. 2(b).

IV. DISCUSSION

One of the biggest challenges of the technological investigation in low dimensions is the instability of the target 2D material. Many materials are stable in bulk but corrode once they are cleaved down to several layers [3,46,47]. The inert hexagonal boron nitride (h-BN) is widely used for encapsulating the 2D vdW materials to prohibit degradation. For example, all reported spintronic devices based on the 2D CrI_3 are covered by h-BN thin flakes to minimize environmental effects [48,49]. However, the weak adhesion of h-BN makes it difficult to adapt to certain 2D materials such as TMX_2 (TM = Ta and Nb, X = S, Se, and Te) [50]. Luckily, the $CrPS_4$ crystal, including the few-layer and monolayer counterpart are stable in the air [20,24,51]. What is more, the few-layer $CrPS_4$ is fabricated to act as the top and bottom protection layers for $NbSe_2$ nanoelectronics [50]. This, therefore, implies that the spintronics built by the 2D $CrPS_4$ could work well without adding any outer protection.

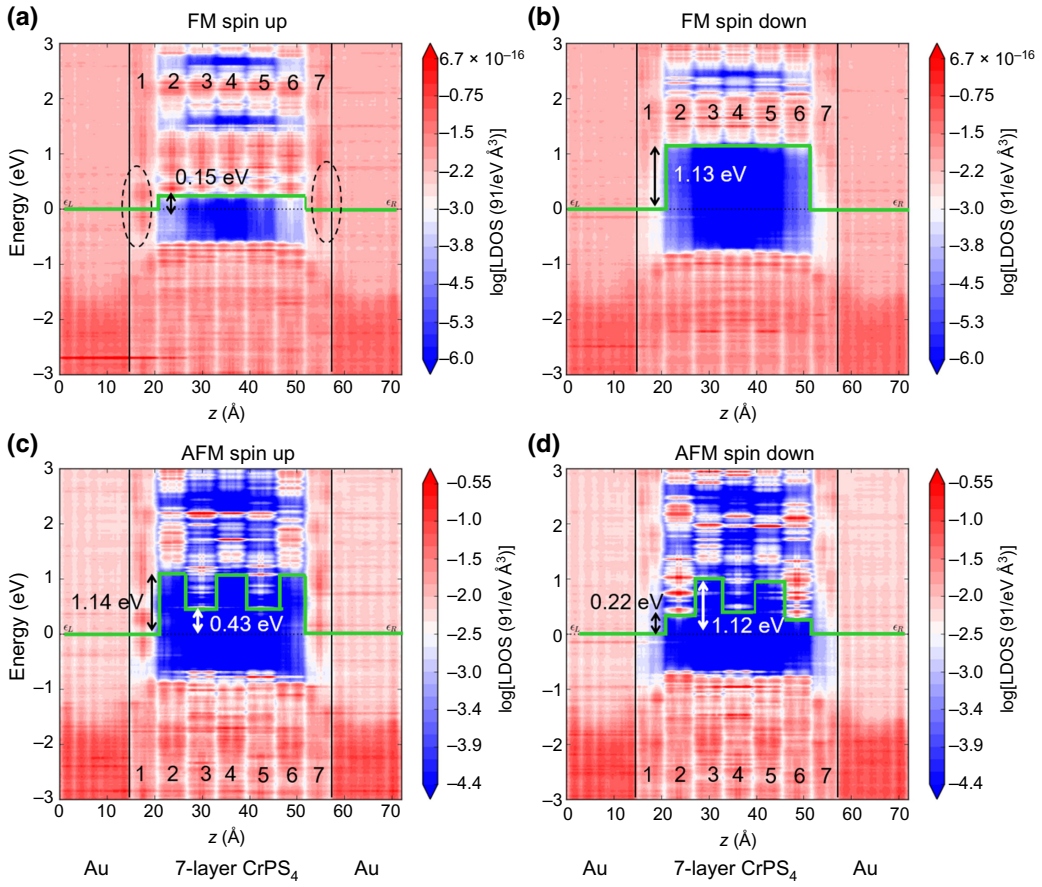

FIG. 7. Spin-resolved projected LDOS of the Au/7-layer $CrPS_4$/Au magnetic tunnel junction for the FM [(a) and (b)] and AFM [(c) and (d)] states. The number marked in (a) indicates the different $CrPS_4$ layer. The Fermi level is zero. The black lines are the boundary of the electrode and tunnel region. The green lines are the spin-dependent potential barrier profile. The LDOS are in the log scale. The barrier heights are labeled.

Compared with the traditional MTJ, the building block and the intrinsic mechanism of our 2D antiferromagnet-based MTJ are different. The traditional MTJ consists of one tunnel region (i.e., Al_2O_3 and MgO) and two ferromagnetic regions—one is the free layer to switch the magnetic alignment along with the external magnetic field, and the other is the pinning layer made up of a ferromagnetic film depositing on an antiferromagnetic film to pin the magnetic structure of the ferromagnetic film depending on their mutual exchange coupling. The maximum TMR record of the traditional MTJs, built by Co-Fe-B and MgO, originates from the different decay rates within the MgO for the different electronic Bloch states in the ferromagnetic electrodes [14,15,39]. Instead of the different multifunctional layers, the kernel of our MTJs is the intrinsic semiconducting and antiferromagnetic 2D $CrPS_4$, which simultaneously provides the tunnel barrier and the magnetic transition. The conductance difference occurs because electrons with different spins experience different tunneling barriers when the magnetic order in $CrPS_4$ switches with the external magnetic field. The MTJs composed of the 2D antiferromagnets open a potential route to achieve 2D spintronics.

As we discuss the ideal spin-resolved transport of the 2D $CrPS_4$-based MTJs, the surprising giant TMR implies a signal that the atomically thin 2D magnets may achieve incredible possibilities, unreachable in the conventional spintronic devices [52]. The magnetic tunnel junctions made up of several-layer $CrPS_4$ and graphene electrodes have been experimentally fabricated, and a high TMR of approximately 300% is observed in the case of an 8-layer $CrPS_4$ MTJ below 38 K and under a strong magnetic field [53]. We believe that the MTJs built by other A-type antiferromagnetic semiconductors might also have similar TMR behavior with large values and layer-increasing tendency. There are plenty of A-type antiferromagnets in the 2D regime, such as $MnBi_2Te_4$, transition-metal oxyhalides (MYX; M = Cr/V/Ti, Y = O/S/Se, X = Cl/Br), and transition-metal trihalides (VX_3; X = Cl/Br/I) [54]. $MnBi_2Te_4$ and CrSBr have scaled down to the monolayer in the experiment [10,55]. Their transport performance lacks

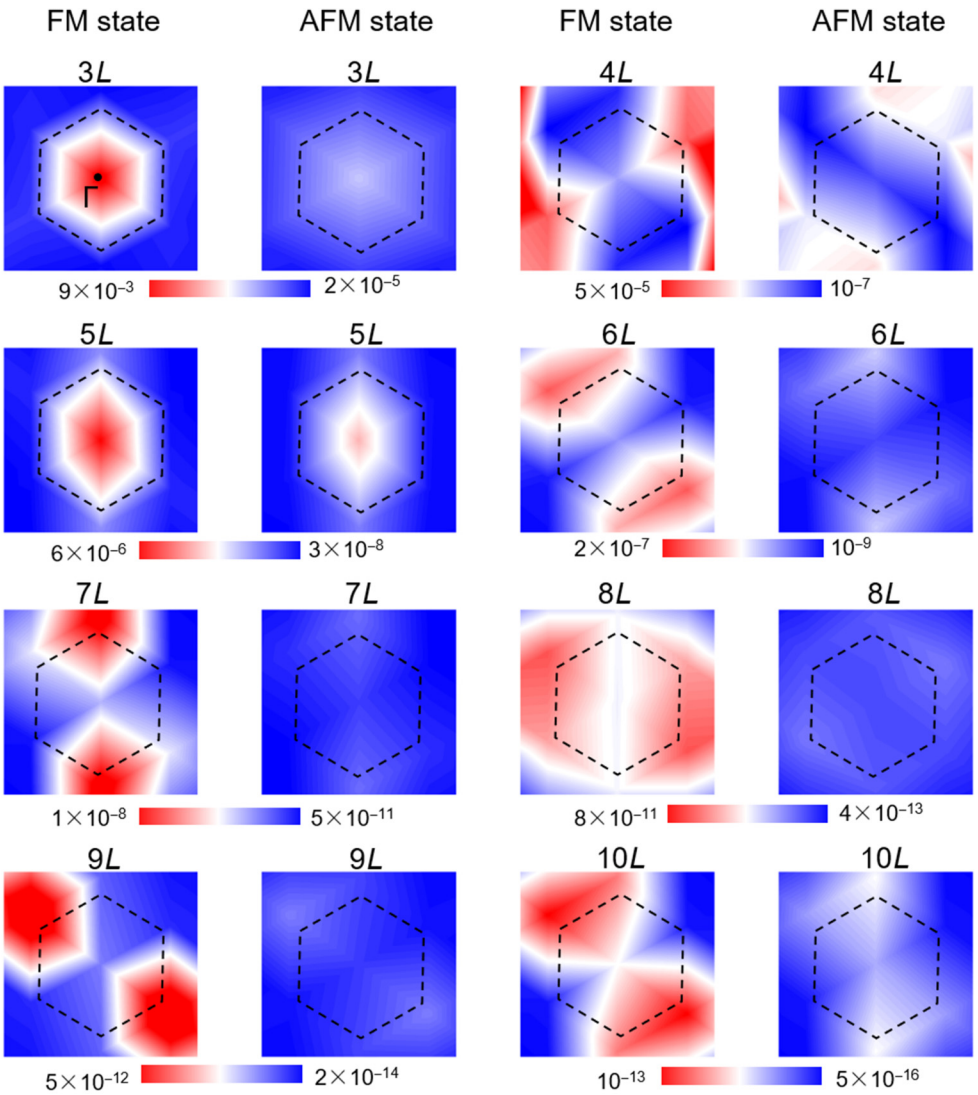

FIG. 8. $k_{\parallel}$-resolved transmission coefficients across the Au/n-layer $CrPS_4$/Au (n is from 3 to 10) magnetic tunnel junction in the Brillouin zone for the FM and AFM state calculated at the Fermi level.

systematic study up to now except for our $CrPS_4$. Further calculations and experiments are highly desirable. Besides, among the class of A-type antiferromagnets, the band structures in the FM state with half-metallic features in or nearby the Fermi level would produce a very large TMR theoretically. A zero tunnel barrier height for the majority spin electrons caused by the half-metallic band structures enhances the transmission probabilities in the FM state and thus the TMR. However, none of them has been found yet.

V. CONCLUSION

In summary, we make a comprehensive study of the layer-dependent TMR of the 2D $CrPS_4$-based MTJs by using the method of *ab initio* quantum-transport simulation. The TMR of the 2D $CrPS_4$-based MTJs generally increases with the increasing layer. It experiences an odd-even oscillation when the tunnel thickness is less than 7 layers and then monotonically increases up to a remarkable value of 370 000% when the tunnel thickness stacks to 10 layers. We explain the relationship between the TMR and the tunnel barrier thickness by using WKB approximation. The calculated giant TMR of the Au/2D $CrPS_4$/Au MTJs allows us to firmly believe in the potential of the 2D antiferromagnets to develop next-generation spintronics.

ACKNOWLEDGMENT

This work is supported by the National Key Research and Development Program of China [Grants No. 2017YFA0206303 and No. 2016YFB0700600 (National Materials Genome Project)], the National Natural Science Foundation of China (Grants No. 11674005, No. 91964101, No. 5173100, and No. 11975035), Open Fund of IPOC (BUPT), High-Performance Computing Platform of Peking University, and MatCloud + high throughput simulation engine.

The authors declare no conflict of interest.

TABLE I. Spin- and layer-dependent band gaps (eV) of 2D $CrPS_4$ in the AFM and FM states.

	2*L*	3*L*	4*L*	5*L*	6*L*	7*L*	8*L*	9*L*	10*L*	Bulk
$\Delta_{AFM,\uparrow}$	0.57	0.55	0.54	0.56	0.53	0.56	0.56	0.31	0.07	0.83
$\Delta_{AFM,\downarrow}$								0.35		
$\Delta_{FM,\uparrow}$	0.69	0.52	0.65	0.64	0.68	0.64	0.64	0.64	0.64	0.72
$\Delta_{FM,\downarrow}$	1.15	1.11	1.10	1.09	1.08	1.08	1.07	1.07	1.07	1.43

APPENDIX

Since Au is used for providing electrons, we speculate that the deformation would not change the order of magnitude of our results. To make a confirmation, we choose an intrinsic 5-layer Au (111) to contact 3-layer $CrPS_4$ without optimization and with the same interlayer distance of approximately 1.67 Å to be a reference group and calculate the transport behavior. Its TMR is approximately 420%, larger than our former calculation results with all Au atoms relaxed (137%) but at the same order of magnitude level. Because the TMR changes by 1 order-of-magnitude with the increasing tunnel barrier thickness, the effect of different relaxation ways (partial relaxation and complete relaxation) of the Au electrode on the TMR is negligible compared with the layer-dependent scaling behavior.

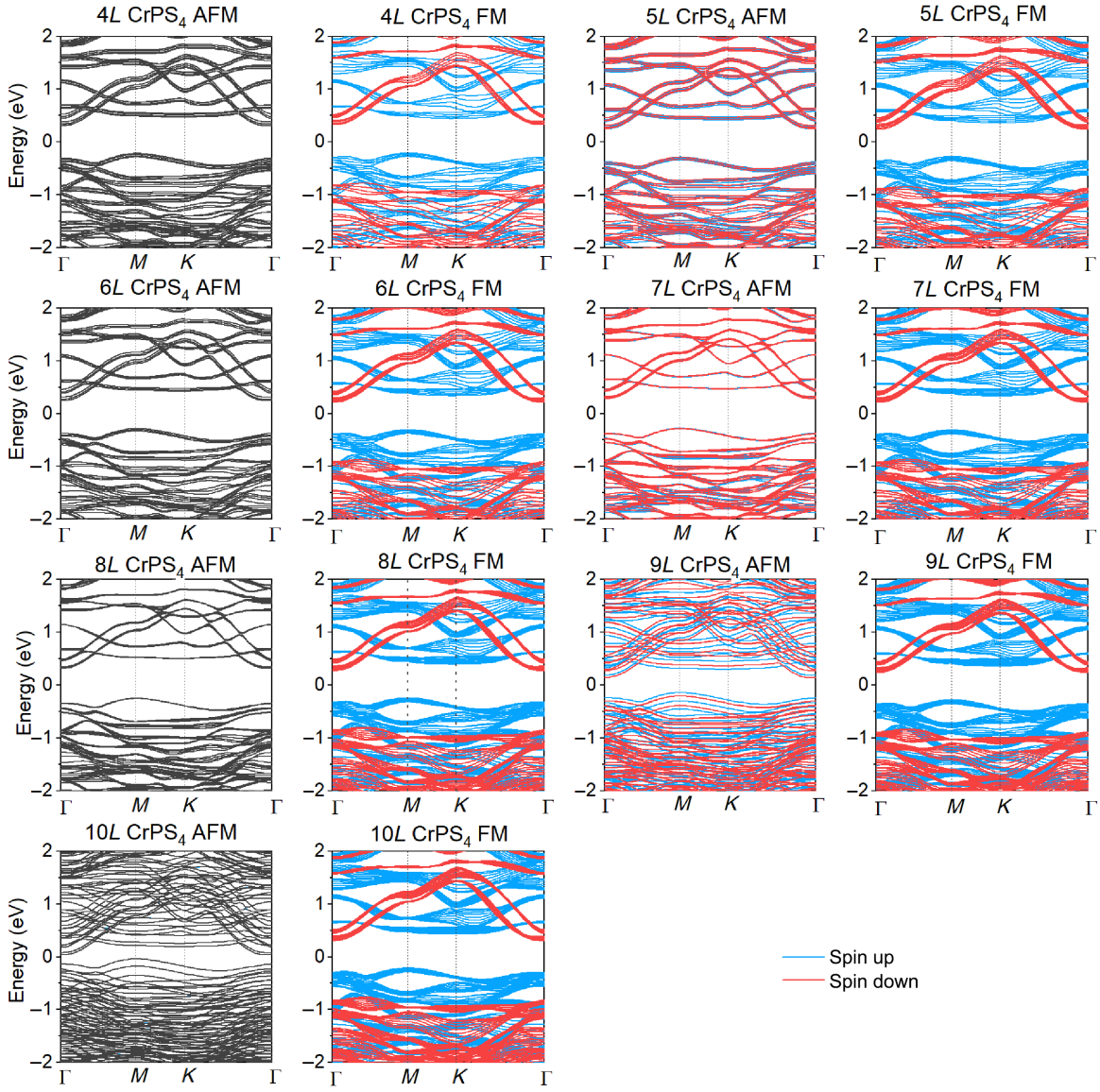

FIG. 9. Spin-resolved band structures of 4 to 10 layers $CrPS_4$ in the AFM and FM states.

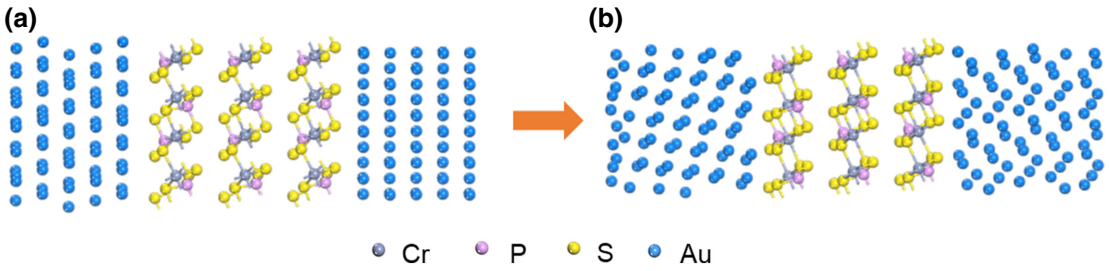

FIG. 10. Lattice structure of the Au/3-layer $CrPS_4$/Au heterostructure before and after geometry optimization.

[1] C. Gong and X. Zhang, Two-dimensional magnetic crystals and emergent heterostructure devices, Science **363**, eaav4450 (2019).

[2] C. Gong, L. Li, Z. Li, H. Ji, A. Stern, Y. Xia, T. Cao, W. Bao, C. Wang, Y. Wang, Z. Q. Qiu, R. J. Cava, S. G. Louie, J. Xia, and X. Zhang, Discovery of intrinsic ferromagnetism in two-dimensional van der waals crystals, Nature **546**, 265 (2017).

[3] Z. Wang, I. Gutiérrez-Lezama, N. Ubrig, M. Kroner, M. Gibertini, T. Taniguchi, K. Watanabe, A. Imamoğlu, E. Giannini, and A. F. Morpurgo, Very large tunneling magnetoresistance in layered magnetic semiconductor CrI_3, Nat. Commun. **9**, 2516 (2018).

[4] D. R. Klein, D. MacNeill, J. L. Lado, D. Soriano, E. Navarro-Moratalla, K. Watanabe, T. Taniguchi, S. Manni, P. Canfield, J. Fernández-Rossier, and P. Jarillo-Herrero, Probing magnetism in 2D van der Waals crystalline insulators via electron tunneling, Science **360**, 1218 (2018).

[5] T. R. Paudel and E. Y. Tsymbal, Spin filtering in CrI_3 tunnel junctions, ACS Appl. Mater. Interfaces **11**, 15781 (2019).

[6] Z. Wang, M. Gibertini, D. Dumcenco, T. Taniguchi, K. Watanabe, E. Giannini, and A. F. Morpurgo, Determining the phase diagram of atomically thin layered antiferromagnet $CrCl_3$, Nat. Nanotechnol. **14**, 1116 (2019).

[7] W. Chen, Z. Sun, Z. Wang, L. Gu, X. Xu, S. Wu, and C. Gao, Direct observation of van der waals stacking–dependent interlayer magnetism, Science **366**, 983 (2019).

[8] Y. Deng, Y. Yu, Y. Song, J. Zhang, N. Z. Wang, Z. Sun, Y. Yi, Y. Z. Wu, S. Wu, J. Zhu, J. Wang, X. H. Chen, and Y. Zhang, Gate-tunable room-temperature ferromagnetism in two-dimensional Fe_3GeTe_2, Nature **563**, 94 (2018).

[9] X. Li, J.-T. Lü, J. Zhang, L. You, Y. Su, and E. Y. Tsymbal, Spin-dependent transport in van der Waals magnetic tunnel junctions with Fe_3GeTe_2 electrodes, Nano Lett. **19**, 5133 (2019).

[10] E. J. Telford, A. H. Dismukes, K. Lee, M. Cheng, A. Wieteska, A. K. Bartholomew, Y.-S. Chen, X. Xu, A. N. Pasupathy, X. Zhu, C. R. Dean, and X. Roy, Layered antiferromagnetism induces large negative magnetoresistance in the van der Waals semiconductor CrSBr, Adv. Mater. **32**, 2003240 (2020).

[11] M. Long, P. Wang, H. Fang, and W. Hu, Progress, challenges, and opportunities for 2D material based photodetectors, Adv. Funct. Mater. **29**, 1803807 (2019).

[12] T. Song, X. Cai, M. W.-Y. Tu, X. Zhang, B. Huang, N. P. Wilson, K. L. Seyler, L. Zhu, T. Taniguchi, K. Watanabe, M. A. McGuire, D. H. Cobden, D. Xiao, W. Yao, and X. Xu, Giant tunneling magnetoresistance in spin-filter van der Waals heterostructures, Science **360**, 1214 (2018).

[13] H. H. Kim, B. Yang, T. Patel, F. Sfigakis, C. Li, S. Tian, H. Lei, and A. W. Tsen, One million percent tunnel magnetoresistance in a magnetic van der Waals heterostructure, Nano Lett. **18**, 4885 (2018).

[14] W. H. Butler, X. G. Zhang, T. C. Schulthess, and J. M. MacLaren, Spin-dependent tunneling conductance of Fe/MgO/Fe sandwiches, Phys. Rev. B **63**, 054416 (2001).

[15] S. Ikeda, J. Hayakawa, Y. Ashizawa, Y. M. Lee, K. Miura, H. Hasegawa, M. Tsunoda, F. Matsukura, and H. Ohno, Tunnel magnetoresistance of 604% at 300 K by suppression of Ta diffusion in CoFeBâĹŢMgOâĹŢCoFeB pseudo-spin-valves annealed at high temperature, Appl. Phys. Lett. **93**, 082508 (2008).

[16] L. Pan, L. Huang, M. Zhong, X.-W. Jiang, H.-X. Deng, J. Li, J.-B. Xia, and Z. Wei, Large tunneling magnetoresistance in magnetic tunneling junctions based on two-dimensional CrX3 (X = Br, I) monolayers, Nanoscale **10**, 22196 (2018).

[17] S. Bhatti, R. Sbiaa, A. Hirohata, H. Ohno, S. Fukami, and S. N. Piramanayagam, Spintronics based random access memory: A review, Mater. Today **20**, 530 (2017).

[18] R. A. Susilo, B. G. Jang, J. Feng, Q. Du, Z. Yan, H. Dong, M. Yuan, C. Petrovic, J. H. Shim, D. Y. Kim, and B. Chen, Band gap crossover and insulator–metal transition in the compressed layered $CrPS_4$, npj Quantum Mater. **5**, 58 (2020).

[19] S. Ding, Y. Peng, M. Xue, Z. Liu, Z. Liang, W. Yang, Y. Sun, J. Zhao, C. Wang, S. Liu, J. Han, and J. Yang, Magnetic phase diagram of $CrPS_4$ and its exchange interaction in contact with NiFe, J. Phys.: Condens. Matter **32**, 405804 (2020).

[20] J. Lee, T. Y. Ko, J. H. Kim, H. Bark, B. Kang, S.-G. Jung, T. Park, Z. Lee, S. Ryu, and C. Lee, Structural and optical properties of single- and few-layer magnetic semiconductor $CrPS_4$, ACS Nano **11**, 10935 (2017).

[21] R. Diehl and C. D. Carpentier, The crystal structure of chromium thiophosphate, $CrPS_4$, Acta Crystallogr., Sect. B **33**, 1399 (1977).

[22] M. Joe, H. Lee, M. M. Alyörük, J. Lee, S. Y. Kim, C. Lee, and J. H. Lee, A comprehensive study of piezomagnetic response in $CrPS_4$ monolayer: Mechanical, electronic properties and magnetic ordering under strains, J. Phys.: Condens. Matter **29**, 405801 (2017).

[23] Q. L. Pei, X. Luo, G. T. Lin, J. Y. Song, L. Hu, Y. M. Zou, L. Yu, W. Tong, W. H. Song, W. J. Lu, and Y. P. Sun, Spin dynamics, electronic, and thermal transport properties of

two-dimensional $CrPS_4$ single crystal, J. Appl. Phys. **119**, 043902 (2016).

[24] Y. Peng, S. Ding, M. Cheng, Q. Hu, J. Yang, F. Wang, M. Xue, Z. Liu, Z. Lin, M. Avdeev, Y. Hou, W. Yang, Y. Zheng, and J. Yang, Magnetic structure and metamagnetic transitions in the van der Waals antiferromagnet $CrPS_4$, Adv. Mater. **32**, 2001200 (2020).

[25] H. L. Zhuang and J. Zhou, Density functional theory study of bulk and single-layer magnetic semiconductor $CrPS_4$, Phys. Rev. B **94**, 195307 (2016).

[26] P. Gu, Q. Tan, Y. Wan, Z. Li, Y. Peng, J. Lai, J. Ma, X. Yao, S. Yang, K. Yuan, D. Sun, B. Peng, J. Zhang, and Y. Ye, Photoluminescent quantum interference in a van der Waals magnet preserved by symmetry breaking, ACS Nano **14**, 1003 (2020).

[27] S. Kim, J. Lee, G. Jin, M.-H. Jo, C. Lee, and S. Ryu, Crossover between photochemical and photothermal oxidations of atomically thin magnetic semiconductor $CrPS_4$, Nano Lett. **19**, 4043 (2019).

[28] Z.-Z. Lin and X. Chen, Ultrathin scattering spin filter and magnetic tunnel junction implemented by ferromagnetic 2D van der Waals material, Adv. Electron. Mater. **6**, 1900968 (2020).

[29] W. Yang, Y. Cao, J. Han, X. Lin, X. Wang, G. Wei, C. Lv, A. Bournel, and W. Zhao, Spin-filter induced large magnetoresistance in 2D van der Waals magnetic tunnel junctions, Nanoscale **13**, 862 (2021).

[30] F. Li, B. Yang, Y. Zhu, X. Han, and Y. Yan, Four distinct resistive states in van der waals full magnetic 1T-VSe_2/CrI_3/1T-VSe_2 tunnel junction, Appl. Surf. Sci. **505**, 144648 (2020).

[31] J. J. Heath, M. Costa, M. Buongiorno-Nardelli, and M. A. Kuroda, Role of quantum confinement and interlayer coupling in CrI_3-graphene magnetic tunnel junctions, Phys. Rev. B **101**, 195439 (2020).

[32] Z. Yan, R. Zhang, X. Dong, S. Qi, and X. Xu, Significant tunneling magnetoresistance and excellent spin filtering effect in CrI_3-based van der Waals magnetic tunnel junctions, Phys. Chem. Chem. Phys. **22**, 14773 (2020).

[33] M. Brandbyge, J.-L. Mozos, P. Ordejon, J. Taylor, and K. Stokbro, Density-functional method for nonequilibrium electron transport, Phys. Rev. B **65**, 165401 (2001).

[34] M. S. José, A. Emilio, D. G. Julian, G. Alberto, J. Javier, O. Pablo, and S.-P. Daniel, The SIESTA method for ab initio order- N materials simulation, J. Phys.: Condens. Matter **14**, 2745 (2002).

[35] G. Kresse and J. Furthmüller, Efficient iterative schemes for ab initio total-energy calculations using a plane-wave basis set, Phys. Rev. B **54**, 11169 (1996).

[36] J. P. Perdew, K. Burke, and M. Ernzerhof, Generalized Gradient Approximation Made Simple, Phys. Rev. Lett. **77**, 3865 (1996).

[37] C. Yang, Z. Song, X. Sun, and J. Lu, Valley pseudospin in monolayer $MoSi_2N_4$ and$MoSi_2As_4$, Phys. Rev. B **103**, 035308 (2021).

[38] H. Zhang, M. Ye, Y. Wang, R. Quhe, Y. Pan, Y. Guo, Z. Song, J. Yang, W. Guo, and J. Lu, Magnetoresistance in Co/2D MoS_2/Co and Ni/2D MoS_2/Ni junctions, Phys. Chem. Chem. Phys. **18**, 16367 (2016).

[39] J. Yang, R. Quhe, S. Liu, Y. Peng, X. Sun, L. Zha, B. Wu, B. Shi, C. Yang, J. Shi, G. Tian, C. Wang, J. Lu, and J. Yang, Gate-tunable high magnetoresistance in monolayer Fe_3GeTe_2 spin valves, Phys. Chem. Chem. Phys. **22**, 25730 (2020).

[40] D. Supriyo, *Quantum Transport: Atom to Transistor* (Cambridge University Press, Cambridge, 2005).

[41] D. C. Worledge and T. H. Geballe, Magnetoresistive double spin filter tunnel junction, J. Appl. Phys. **88**, 5277 (2000).

[42] Y. B. Band and Y. Avishai, *Quantum Mechanics with Applications to Nanotechnology and Information Science* (Academic Press, Amsterdam, 2013), pp. 303–366.

[43] H. Zhou, Y. Zhang, and W. Zhao, Tunable tunneling magnetoresistance in van der Waals magnetic tunnel junctions with 1T-$CrTe_2$ electrodes, ACS Appl. Mater. Interfaces **13**, 1214 (2021).

[44] L. Pan, H. Wen, L. Huang, L. Chen, H.-X. Deng, J.-B. Xia, and Z. Wei, Two-dimensional XSe2 (X = Mn, V) based magnetic tunneling junctions with high Curie temperature, Chin. Phys. B **28**, 107504 (2019).

[45] K. Sankaran, J. Swerts, S. Couet, K. Stokbro, and G. Pourtois, Oscillatory behavior of the tunnel magnetoresistance due to thickness variations in Ta|CoFe|MgO magnetic tunnel junctions: A first-principles study, Phys. Rev. B **94**, 094424 (2016).

[46] A. K. Geim and I. V. Grigorieva, Van der Waals heterostructures, Nature **499**, 419 (2013).

[47] A. Carvalho, M. Wang, X. Zhu, A. S. Rodin, H. Su, and A. H. Castro Neto, Phosphorene: From theory to applications, Nat. Rev. Mater. **1**, 16061 (2016).

[48] G. Qiu, M. Si, Y. Wang, X. Lyu, W. Wu, and P. D. Ye, in *2018 76th Device Research Conference (DRC)* (2018), pp. 1–2.

[49] S. Jiang, L. Li, Z. Wang, K. F. Mak, and J. Shan, Controlling magnetism in 2D CrI_3 by electrostatic doping, Nat. Nanotechnol. **13**, 549 (2018).

[50] S. Son, Y. J. Shin, K. Zhang, J. Shin, S. Lee, H. Idzuchi, M. J. Coak, H. Kim, J. Kim, J. H. Kim, M. Kim, D. Kim, P. Kim, and J.-G. Park, Strongly adhesive dry transfer technique for van der waals heterostructure, 2D Mater. **7**, 041005 (2020).

[51] S. Calder, A. V. Haglund, Y. Liu, D. M. Pajerowski, H. B. Cao, T. J. Williams, V. O. Garlea, and D. Mandrus, Magnetic structure and exchange interactions in the layered semiconductor $CrPS_4$, Phys. Rev. B **102**, 024408 (2020).

[52] Z. Wang, D. Sapkota, T. Taniguchi, K. Watanabe, D. Mandrus, and A. F. Morpurgo, Tunneling spin valves based on Fe_3GeTe_2/hBN/Fe_3GeTe_2 van der waals heterostructures, Nano Lett. **18**, 4303 (2018).

[53] Y. Zheng, Transport behavior of $CrPS_4$ MTJs, (unpublished).

[54] S. Son, M. J. Coak, N. Lee, J. Kim, T. Y. Kim, H. Hamidov, H. Cho, C. Liu, D. M. Jarvis, P. A. C. Brown, J. H. Kim, C.-H. Park, D. I. Khomskii, S. S. Saxena, and J.-G. Park, Bulk properties of the van der Waals hard ferromagnet VI_3, Phys. Rev. B **99**, 041402 (2019).

[55] S. Yang, X. Xu, Y. Zhu, R. Niu, C. Xu, Y. Peng, X. Cheng, X. Jia, Y. Huang, X. Xu, J. Lu, and Y. Ye, Odd-even layer-number effect and layer-dependent magnetic phase diagrams in $MnBi_2Te_4$, Phys. Rev. X **11**, 011003 (2021).